Available online at www.sciencedirect.com
ScienceDirect
International Journal of Heat and Mass Transfer 50 (2007) 5283–5291
International Journal of HEAT and MASS TRANSFER
www.elsevier.com/locate/ijhmt

Interfacial thermocapillary pressure of an accelerated droplet in microchannels: Part II. Heat transfer formulation

P.S. Glockner [a], G.F. Naterer [b,*]

[a] Nova 3 Engineering Ltd. 201-120 Fort Street Winnipeg, Manitoba, Canada, R3C1C7
[b] Faculty of Engineering and Applied Science, University of Ontario Institute of Technology, 2000 Simcoe Street North, Oshawa, Ontario, Canada L1H 7K4

Received 11 August 2006; received in revised form 6 April 2007
Available online 15 August 2007

Abstract

In this companion paper of a two-paper set of thermocapillary pumping studies, a heat transfer formulation is developed with thermal convection in the microchannel and heat conduction in the substrate. Unlike past studies based on a uniform pressure along the droplet/air interface, this article incorporates a more realistic interfacial pressure/velocity coupling to better predict temperature variations along the moving boundary. This improves predictions of thermocapillary forces at the interface, which drive the droplet motion within the microchannel. Close agreement between approximate and numerical predictions of droplet temperature and displacement provide useful validation of the models.

1. Introduction

MEMS and nanotechnology have enormous potential for the development of novel materials, devices and systems through control of matter at the micro or nanometer length scale (1–100 nm). Theses technologies exploit novel phenomena and properties (chemical, biological, mechanical, electrical and so forth) at very small length scales. For comparison purposes, 1 nm is about 10,000 times smaller than the diameter of a human hair. The fabrication of novel micro and nano-devices is rapidly gaining worldwide attention, due to its promising potential in various technological applications. The opportunity of fabricating ultrasmall structures opens a wide range of potential commercial applications. Experts at the US National Science Foundation have suggested that the value of the worldwide commercial market for nanotechnology products may reach $1 trillion or higher between 2010 and 2015. Many financial investors from around the world expect that MEMS and nanotechnology will become an important contributor to the world economy. A large nanotechnology R&D infrastructure is currently established at many universities and research institutes around the world, but the commercial markets will likely become much larger in the near future.

Micro-electromechanical systems (MEMS) refer to the integration of mechanical components, electronics, sensors and actuators into a common device at the micrometer scale. Although MEMS involves devices and systems that are one thousand times larger than nanotechnology, they offer promising alternatives to conventional technologies. MEMS technology has contributed significantly in applications to sensors, computer peripherals, actuators and various others. Some specific examples of innovative micro-devices are accelerometers for automobile airbags, keyless entry systems, dense arrays of optical mirrors for high-definition optical displays and scanning electron microscope tips to visualize single atoms. MEMS have also been applied in biomedical applications, such as microsystems for separating biological cells, blood analyzers and pressure transducers for catheters. Micro-heat exchangers have been developed for convective cooling of microelectronic circuits [1,2]. Effective microscale heat and fluid

* Corresponding author. Tel.: +1 9057213111; fax: +1 9057213370.
E-mail address: greg.naterer@uoit.ca (G.F. Naterer).

0017-9310/$ - see front matter © 2007 Elsevier Ltd. All rights reserved.
doi:10.1016/j.ijheatmasstransfer.2007.06.017

Nomenclature

A	interfacial area (m^2)
c_p	specific heat (J/kg K)
h	convection coefficient (W/m^2 K)
k	thermal conductivity (W/m K)
P	pressure (Pa)
q''	heat flux (W/m^2)
S	source term
t	time (s)
T	temperature (K)
u, v	x and y-velocity components (m/s)
V	volume (m^3)
x, y	Cartesian coordinates (m)

Greek symbols

α	thermal diffusivity (m^2/s)
μ	dynamic viscosity (kg/ms)
ρ	density (kg/m^3)

Subscripts

a	air
CV	control volume
d	droplet
e, w	east, west integration points
E, W, P	east, west, central nodal points
i	initial
L, R	left edge, right edge
s	supply

exchange are key enabling technologies for micro-heat engines [3], micro-valves [4] and micro-spacecraft [5]. Surface micro-patterning with EBSM (entropy based surface micro-profiling; [6]) enables flow control in convective heat transfer problems, while simultaneously reducing entropy production through slip-flow drag reduction of open microchannel networks embedded within the surface.

Electro-osmosis (electrically driven flow) is a common method of transporting fluids through microdevices and microchannels. An externally applied electric field produces a net force on the fluid [7]. The electric field can be manipulated along the walls of a microchannel to control the speed and direction of fluid motion. The charged surface attracts ions of the opposite charge in the surrounding fluid, thereby leading to an electric double layer (EDL) near the wall [8]. Axial variations in cross-sectional properties of the microchannel can produce a secondary flow, which limits the rate of electrophoretic separation [9]. Electrokinetic transport through microchannels has been studied numerically by Glockner and Naterer [10]. Electromagnetic forces contribute to entropy production within the microchannel [11], which limits operating performance by dissipating kinetic energy to internal energy [12,13].

Unlike electro-osmosis, electrocapillary transport uses an electrical potential gradient between two immiscible conducting fluids to generate a spatial change of surface tension. The resulting fluid motion is called continuous electrowetting (CEW). Lee and Kim [14] have studied CEW control with a micro-droplet of liquid metal in a circular microchannel. Using an applied voltage of 2.8 V and a micromotor, the authors reported that liquid metal droplets can be transported along a microchannel loop in an electrolyte. Difficulties involving material compatibility, electrode polarization and electrolysis were documented by the authors.

Yun et al. [15] studied droplet motion through a microchannel on a glass wafer, which was filled with an electrolyte containing the droplet. The moving droplet drags the electrolyte, thereby deflecting a membrane on a second adjoining silicon wafer. Inlet and outlet chambers on another silicon wafer were connected with a tube to complete the micro-pump loop. The configuration allowed a maximum pump pressure of 800 Pa, with an applied voltage of 2.3 V at an operating frequency of 25 Hz and power consumption of 170 W.

Unlike the previous methods of flow control in microchannels, thermocapillary pumping takes advantage of thermocapillary forces, which arise when variations of surface tension and differences between contact angles at both ends of a droplet or liquid film contribute to an effective pressure difference across the liquid. Thermocapillary pumping (TCP) was discussed in the previous companion paper. The purpose of this paper is to develop a new understanding of heat transfer near the droplet/air interface of droplets pumped by thermocapillarity in microchannels. The thermal conductivity and substrate thickness affect the rate of thermocapillary heat transfer in microchannels. Sammarco and Burns [16,17] investigated droplet interface temperatures at droplet velocities below about 1 mm/s for pumping of a water droplet on a silica substrate material. This article studies a similar process, but instead for a closed-end microchannel, with a non-uniform droplet/air interface pressure and stationary (rather than moving) heat source.

Ghiaasiaan and Chedester [18,19] reported that thermocapillary forces suppress microbubbles forming in wall cavities of microchannels. The authors suggested that incipience in microchannels can be effectively controlled by thermocapillary action. The onset of significant void in microtubes occurs with bubble departure from wall

cavities, which may be controlled by thermocapillary forces acting on the bubble [20].

Thermocapillary heat transfer in a thin liquid film on a horizontal stretching sheet was investigated analytically with a similarity solution by Dandapat et al. [21]. Fluids with a Prandtl number (Pr) between 0.001 and 100 were considered. For $Pr < 10$, the film thickness and Nusselt number increased. A maximum local velocity occurs within the film, when the thermocapillary forces drag the liquid film along the stretching sheet. As thermocapillary forces diminish, the thermal boundary layer becomes confined to the lower part of the liquid film.

The critical wave number depends on thermocapillary forces in Marangoni instabilities of evaporating droplets [22]. The boundary layer near the free surface of the droplet induces cellular motion because of the Marangoni instabilities. When surface tension decreases with temperature, the thermocapillary and diffuse-capillary effects augment each other. In microchannels, thermocapillary forces provide a promising method of controlling fluid transport of discrete droplets. But effectively optimizing the droplet properties, heat input and wall properties requires detailed understanding of heat transfer within the discrete droplet. This article extends the previous companion paper to develop a detailed heat transfer formulation of an accelerating droplet in a closed microchannel. The following assumptions are adopted in the heat transfer formulation: (i) two-dimensional laminar flow in a rectangular microchannel, (ii) heat transfer without droplet evaporation, breakup or deformation and (iii) negligible effects of electromagnetic fields and wall roughness.

2. Analytical formulation of heat transfer

Fig. 1 illustrates the problem schematic and a sample mesh discretization in the compressed air region. Heat is transferred to a droplet in a closed microchannel from an external heat source, through a thermal bridge embedded in a substrate. Thermocapillary forces on the droplet induce fluid motion within the microchannel. When the droplet moves from left to right in Fig. 1, the air pressure increases in the right section of the microchannel. After a specified period, the heat source is turned off and the droplet moves back towards its initial equilibrium position. A detailed analytical solution for this transient problem is unavailable in the archival literature (to our knowledge). Note that each of the four phase regions (left air region, droplet, right air region and silicon substrate region) has different thermophysical properties. Heat transfer occurs within the liquid, solid and gas regions by coupled heat conduction and thermal convection.

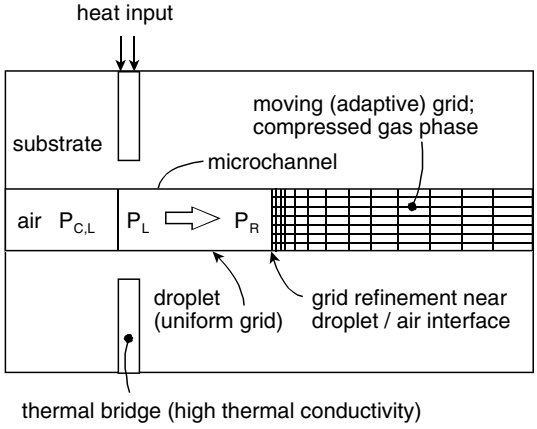

Fig. 1. Schematic of problem domain and mesh discretization for adaptive grid.

An approximate analytical model of droplet heat transfer will be developed in this section. Convective cooling at the interface between the substrate and its surroundings is assumed small compared to axial conduction across the domain, so the droplet/air regions will be approximated by two adjacent quasi one-dimensional semi-infinite regions. Also, the heater is assumed to span the entire height of the microchannel in Fig. 1 and each semi-infinite region has its own heat source at the interface. Then, each region has the same interface temperature and the sum of heat flows from each region balances the total supplied heat flow from the thermal bridge. The interface temperature of either semi-infinite region, subject to a constant interfacial (surface) heat flux, q''_s, becomes

$$T(0,t) = T_i + \frac{2q''_s(\alpha t/\pi)^{1/2}}{k}. \tag{1}$$

This equation can be written for both left and right sides of the heater, yielding two separate temperatures that can be subsequently equated at the interface to give the following result:

$$q''_{s,L}\frac{(\alpha_L)^{1/2}}{k_L} = q''_{s,R}\frac{(\alpha_R)^{1/2}}{k_R}. \tag{2}$$

The sum of heat flows from each region balances the total supplied heat flux from the thermal bridge,

$$q''_{s,R} = q''_s - q''_{s,L}. \tag{3}$$

Combining Eqs. (2) and (3),

$$q''_{s,L} = \frac{q''_s(\alpha_R)^{1/2}/k_R}{(\alpha_L)^{1/2}/k_L + (\alpha_R)^{1/2}/k_R}. \tag{4}$$

This equation yields $q''_{s,L}$ after q''_s is specified, then $q''_{s,R}$ can be solved with Eq. (3). This approximate solution allows heat conduction within the domain to be modeled as two separate problems, with a temperature matching condition at the interface. The previous analysis considered heat transfer to the droplet from the thermal bridge during a heating period, when the heat source is turned on. In order to generate cyclic droplet motion with the droplet returning back to its initial position, the heater must be turned off, otherwise the droplet cannot return back against thermocapillary forces. Thus, a second portion of the approximate

analytical model will be developed for the cooling period, when the heater is turned off.

In the theoretical model, the semi-infinite approximation is used during the heating period when the droplet moves from left to right, but not the subsequent cooling period when the droplet returns back leftwards to its initial position. During this cooling period, a non-uniform temperature distribution and unknown transient surface temperature/heat flux make a semi-infinite assumption unrealistic. The lumped capacitance approximation neglects spatial temperature variations within the droplet, but predicts temporal changes of the receding edge temperature over time during the cooling period. This assumption is assumed reasonable, due to the tiny thermal mass of the microdroplet. Numerical simulations of the full Navier–Stokes and energy equations within the droplet will be performed to assess validity of the lumped capacitance approximation. Using the lumped capacitance assumption during cooling of the droplet [13],

$$T = T_0 + (T_\mathrm{i} - T_0)\exp\left[-\frac{hA_\mathrm{s}t}{\rho V c_\mathrm{p}}\right] \tag{5}$$

which can be re-written as

$$t = \frac{\rho V c_\mathrm{p}}{hA_\mathrm{s}}\ln\left(\frac{T_\mathrm{i} - T_0}{T - T_0}\right), \tag{6}$$

where T_i is the initial temperature in the cooling period and A_s is the surface area exposed to the surroundings with a heat transfer coefficient of h at a temperature of T_0. The heat transfer coefficient, h, was approximated from the heating temperature profile of Eq. (1). The heating profile was considered in reverse, as a cooling curve from the point (T_c, t_c) to (T_i, 0), where the subscript c refers to a critical point when the droplet has been displaced by a specified amount. This model is an approximation and additional accuracy can be obtained through a numerical solution of the coupled Navier–Stokes and energy equations (next section).

3. Numerical formulation of heat transfer

In the previous companion paper of this two-paper set, a finite volume method was developed to solve the Navier–Stokes equations of fluid motion within the droplet. In this section, the same finite volume method will be used, but extended to analyze heat transfer in the droplet, air and substrate regions. The governing energy equations in the droplet and substrate are given by

$$\frac{\partial}{\partial t}(\rho c_\mathrm{p}T) + \frac{\partial}{\partial x}(\rho c_\mathrm{p}uT) + \frac{\partial}{\partial y}(\rho c_\mathrm{p}vT) = \frac{\partial}{\partial x}\left(k\frac{\partial T}{\partial x}\right) + \frac{\partial}{\partial y}\left(k\frac{\partial T}{\partial y}\right) \quad \text{(droplet)}, \tag{7}$$

$$\frac{\partial}{\partial t}(\rho c_\mathrm{p}T) = \frac{\partial}{\partial x}\left(k\frac{\partial T}{\partial x}\right) + \frac{\partial}{\partial y}\left(k\frac{\partial T}{\partial y}\right) \quad \text{(substrate)}, \tag{8}$$

where T in Eqs. (7) and (8) refers to the temperature in the droplet and substrate, respectively. Spatial discretization of the energy equation involves a finite volume mesh with nodes at the center of each control volume (discussed in previous companion paper).

The temperature field within the droplet depends on heat flows from the surrounding air and substrate regions. The interfacial condition of heat transfer at the phase interface (between droplet, d, and air, a) is

$$\left(k\frac{\partial T}{\partial x_\mathrm{i}}\right)_\mathrm{d} = \left(k\frac{\partial T}{\partial x_\mathrm{i}}\right)_\mathrm{a}. \tag{9}$$

Eq. (5) cannot be readily applied as an interfacial condition when using full width control volumes, so a zero width control volume was implemented for the interfacial flux calculations (see Fig. 2). The zero-width control volumes (10^{-32} m thickness in the numerical code) were used along all control volume edges at the droplet/air, droplet/substrate and air/substrate interfaces. These control volumes successfully enforce Eq. (9) without special modeling when generating the temperature coefficient matrices. An energy balance based on Eq. (9) is formulated for the P control volume in Fig. 2 as follows:

$$k_\mathrm{W}\frac{T_\mathrm{P} - T_\mathrm{W}}{(\mathrm{d}x)_\mathrm{w}} = k_\mathrm{E}\frac{T_\mathrm{E} - T_\mathrm{P}}{(\mathrm{d}x)_\mathrm{e}}. \tag{10}$$

Although the temperature field within each region is solved simultaneously with the same coefficient matrices, each

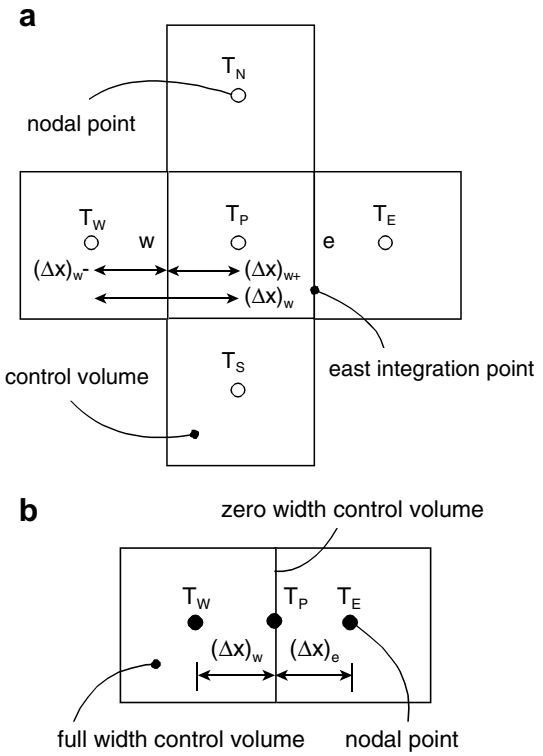

Fig. 2. (a) Full width and (b) zero width control volumes at phase boundary.

region receives slightly different treatment when generating the coefficient matrices.

Heat transfer by conduction is predicted within the substrate. Boundary conditions are applied along the left, lower, and right boundaries of the substrate, while the upper boundary is handled by an interfacial condition analogous to Eq. (9) (note: subscript "a" is replaced by "s", substrate). Also, another algorithm was developed to search the domain and determine the control volumes encompassing the lateral edges of the thermal bridge. All control volumes completely contained within the thermal bridge have the following special boundary condition. A weighted average temperature is specified along the edge of the control volumes that contain the edges of the thermal bridge, i.e.,

$$T = \left(\frac{L_B}{L_{CV}}\right) T_B + \left(\frac{L_{CV} - L_B}{L_{CV}}\right) T_{CV}^{old}, \tag{11}$$

where L_B is the length of the thermal bridge within the control volume, L_{CV} is the length of the control volume and T_{CV}^{old} is the boundary temperature of the control volume from the previous time step. An alternative approach with Neumann conditions was also tested, whereby the heat flux was scaled relative to the fraction of the control volume in contact with the heat source, i.e.,

$$q'' = \left(\frac{L_B}{L_{CV}}\right) q''_{spec}, \tag{12}$$

where q''_{spec} is a specified heat flux between the heat source and the thermal bridge.

The temperature field for all four phase regions (droplet, two air regions and the substrate) is predicted on a single temperature mesh that is separate from the momentum mesh used to predict fluid motion. The pressure nodal points from the momentum mesh are located at the same points as the nodal points from the temperature mesh. The mesh within the substrate is horizontally aligned with the three adjacent grids in the microchannel. After the droplet moves within the microchannel, the temperature mesh is regenerated. The droplet portion of the mesh translates and remains beneath the momentum mesh. The mesh in the upstream air chamber is stretched to accommodate the droplet translation, while simultaneously the grid in the downstream air chamber is compressed. The substrate mesh is distorted to maintain alignment with the control volumes in the microchannel.

The predicted velocity field on the momentum grid, minus the bulk droplet velocity, is used for the advection terms in Eq. (7). Any air flowing out of a control volume within a time step is "reclaimed" by the control volume, when the mesh is re-generated and the control volume is shifted. The convection terms of the energy equation were not included for the air region because no air crosses the edge of a control volume. The newly predicted temperature fields for the droplet and air are located on the updated temperature mesh and they require no adjustment when the mesh is updated, because the fluids within these regions move at the local bulk speed of their respective control volumes. The substrate is a solid, so there is no internal fluid flow and the temperature mesh within the substrate needs to be updated with each time step.

Misalignment along the solid/fluid interface occurs if mesh regeneration is not performed. In order to ensure grid alignment between phases, the mesh within the substrate must be updated after each time step, so it remains aligned with the fluid grids. This requires that the temperature field is updated on the new mesh after each time step. The temperature field in most parts of the new substrate mesh is linearly interpolated from the old temperature field and nodal point locations. Special attention is required near the thermal bridge, where control volumes are composed of several materials and they have composition changes with each time step. The assumption of a constant heat flux through these composite control volumes will be made to approximate the temperature profile between nodal points. The substrate temperature, T_N, corresponding to the new x-location, x_N, is

$$T_N = T_L + \sum_{k=1}^{5} \left[\frac{l_k}{L_k}\frac{R_k}{R_{tot}}(T_R - T_L)\right], \tag{13}$$

where T_L and T_R represent the left and right nodal temperatures bounding T_N. Also, l/L is the fraction of each composite region "overtaken", R_k is the thermal resistance of a particular region and R_{tot} is the total thermal resistance between nodal points. In the next section, predicted results from this numerical formulation will be presented.

4. Results and discussion

This section investigates heat transfer in the microchannel problem corresponding to case (iii) of the previous companion paper. Thus, the fluid and thermal aspects are coupled, whereby the fluid flow results were examined in Part I, while the focus in Part II is the heat transfer results. Problem parameters and thermophysical properties of the droplet, air and substrate are shown in Table 1. In Fig. 3, analytical predictions of the droplet edge temperature

Table 1
Thermophysical properties and problem parameters

Property	Value
Density of droplet	998 kg/m^3
Thermal conductivity of droplet	0.606 W/m K
Specific heat of droplet	4181 J/kg K
Viscosity of droplet	595×10^{-6} N s/m^2
Density of air	1.1614 kg/m^3
Thermal conductivity of air	0.0623 W/m K
Specific heat of air	1007 J/kg K
Density of substrate	2500 kg/m^3
Thermal conductivity of substrate	0.96 W/m K
Specific heat of substrate	837 J/kg K
Channel length	2 mm
Channel height	20, 200, 2000 nm
Channel depth	100 μm

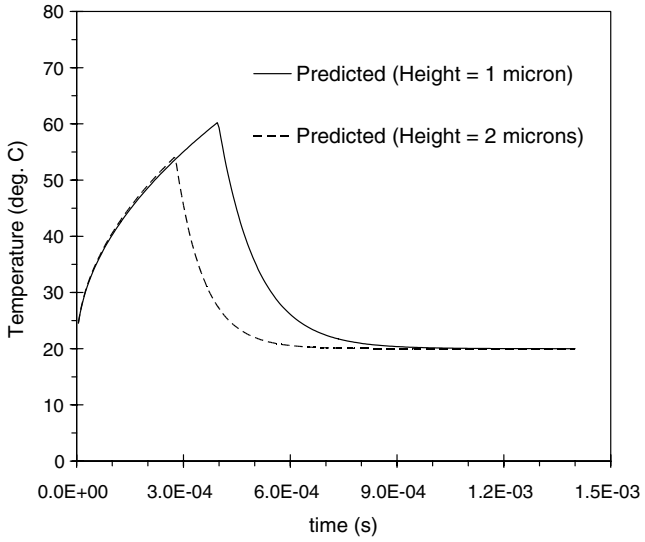

Fig. 3. Droplet interface temperature at varying channel heights.

are shown during a single cycle of the heating/cooling period. It can be observed that the droplet temperature increases when its receding edge is heated, but then decreases after the heat source is turned off during the cooling period. The results in Fig. 3 indicate that the left edge of the droplet reaches a higher peak temperature for the smaller microchannel ($H = 1$ μm). This occurs due to a longer heating period required for the smaller droplet to reach a given displacement, as a result of increased internal friction.

In Fig. 4, analytical predictions of the left droplet edge temperature are compared against numerical predictions. Both Neumann and Dirichlet conditions at the substrate interface yield similar results during the heating period. Close agreement between analytical and numerical predictions is obtained at early stages of time. At early times, the semi-infinite approximation of the analytical model is more realistic because thermal effects of the adjoining gas region are not propagated upstream into the droplet. However, this approximation becomes less accurate as time advances and the droplet decelerates at the end of the heating period. Higher discrepancy between analytical and numerical results is observed during the cooling period after about 0.00039 s, due to inaccuracies in the lumped-capacitance approximation that arise from variations in the heat transfer coefficient and droplet temperature. Despite some discrepancy, fair agreement with underlying trends between the numerical and analytical models provides useful validation of both models, since they were developed independently and still exhibit reasonably close agreement. Such agreement is useful since relevant archived experimental data is unavailable (to our knowledge) for other validation purposes.

The heat transfer model in Section 2 predicted a 1-D spatial variation of temperature in the droplet during the heating period, but only a single bulk temperature in the cooling period. In contrast, the numerical model (Section 3) predicts the 2-D transient change of temperature within

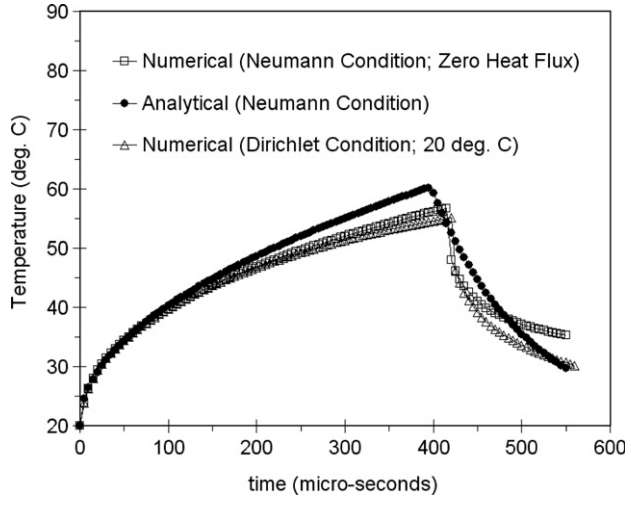

Fig. 4. Numerical (finite volume method) and analytical temperature predictions.

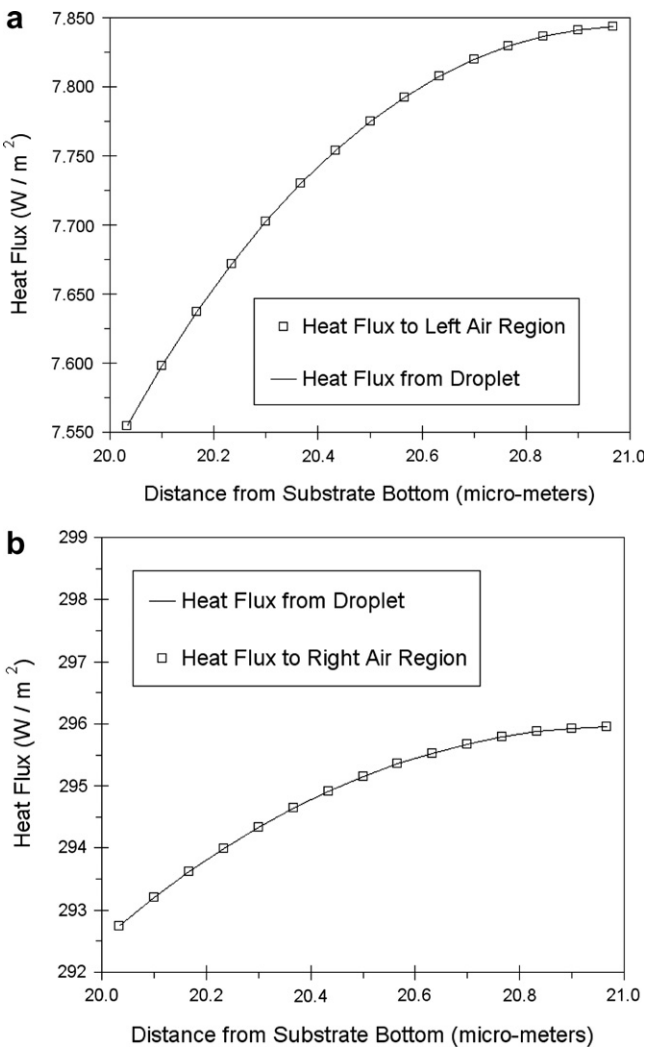

Fig. 5. Convective heat flux at the droplet/air interface.

the droplet, including temperature changes driven by the non-uniform interfacial pressure described in the previous companion paper. Unlike past studies assuming a constant interface pressure and temperature, Fig. 5 shows new results confirming that the heat flux varies along the droplet/air interface, due to convective recirculation which causes a temperature rise from the bottom to top edges of the droplet interface. Fig. 5 illustrates that the heat fluxes match each other on both sides of the interface (as required).

The varying interfacial heat fluxes in Fig. 5 lead to varying temperatures along the advancing (Fig. 6a) and receding edges (Fig. 6b) of the droplet/air interface. In Fig. 6a, the temperature rises upwards along the interface and reaches a zero transverse gradient in the centerline, due to symmetry of the temperature profile about the midplane of the microchannel. In contrast, the temperature decreases upwards at the receding edge of the droplet in Fig. 6b, due to the convective recirculation cell described in the previous companion paper. The droplet temperatures are illustrated at a single node interior to the droplet/air interface. Fig. 6a shows that droplet temperature exceeds the interface and air temperatures, thereby confirming heat transfer from the heated droplet to the upstream air region. It should be noted that small temperature differences are predicted along the vertical axes in Fig. 6a–b. Although these temperature changes appear small, they are sufficiently different to contribute to thermocapillary forces and droplet motion within the microchannel.

When the compressed volume of the air section is reduced, the pressure increases according to the ideal gas law, i.e. $P \propto 1/(950 \times 10^{-6}\Delta x)$. The droplet displacements, Δx, considered in this article are small, relative to the gas chamber length. As a result, a nearly linearly increasing magnitude of the leftward (negative) force is generated on the micro-droplet. In Fig. 7, the horizontal axis refers to the displacement of the interface into the compressed gas section of the microchannel. The force is the gas pressure multiplied by the interfacial area of the micro-droplet. It can be observed that the magnitude of this force increases with larger microchannels, as the pressure difference caused by a specified displacement represents a larger area when the height of the microchannel increases. Negative values are shown in Fig. 7, since the pressure force acts leftwards against the direction of droplet motion. In Fig. 7, fairly close agreement between analytical and numerical predictions (FVM; finite volume method) is illustrated for the 2 μm channel in both heating and cooling periods. These comparisons provide useful validation of the numerical model.

Additional sensitivity studies with the analytical model are illustrated in Fig. 8 for the net force on the moving droplet. The predicted thermocapillary, friction and external air forces are illustrated during a heating/cooling cycle for a 0.5-μm channel (Fig. 8a) and 2-μm channel (Fig. 8b). Larger forces are observed in Fig. 8a (smaller channel height), since larger temperature rises and thermocapillary forces occur when the same heat input is transferred to a smaller droplet. In Fig. 8, a rising droplet temperature produces a higher thermocapillary force, while an opposite trend occurs with a decreasing temperature during the cooling period. A higher thermocapillary force generates a larger pressure gradient and fluid friction. Thus, friction

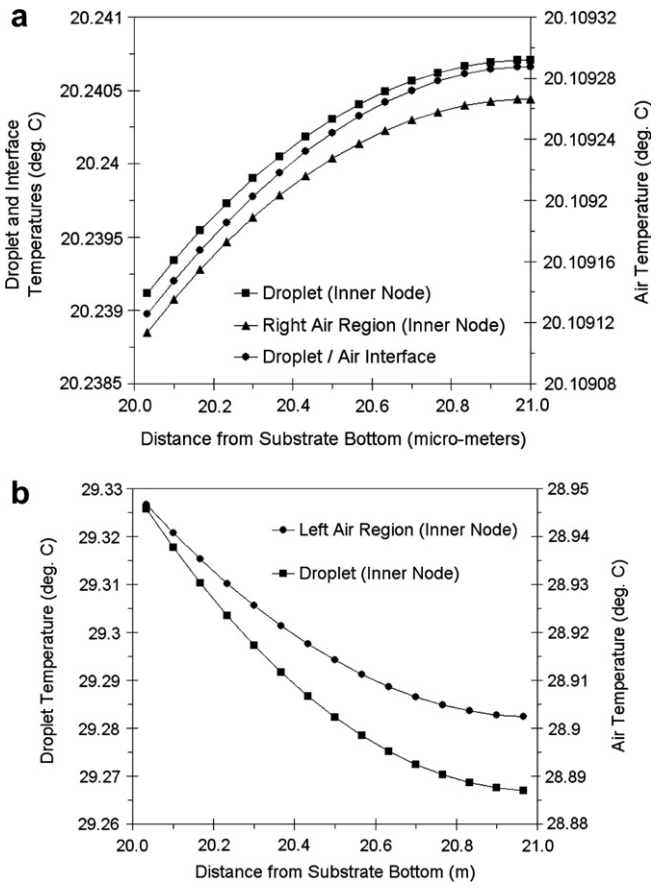

Fig. 6. Predicted temperatures near the (a) right and (b) left droplet/air interface.

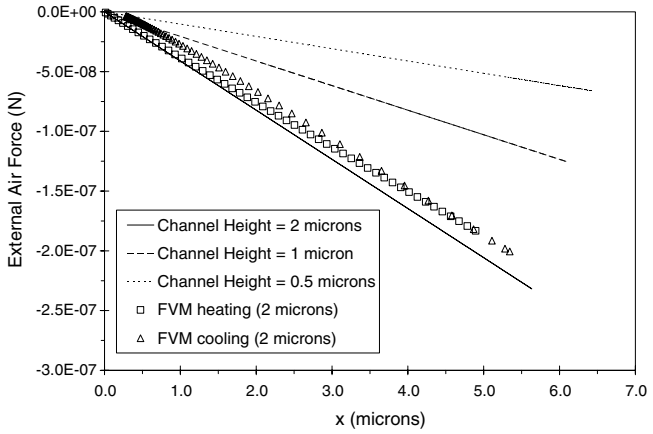

Fig. 7. Predicted change of external air force in closed microchannel.

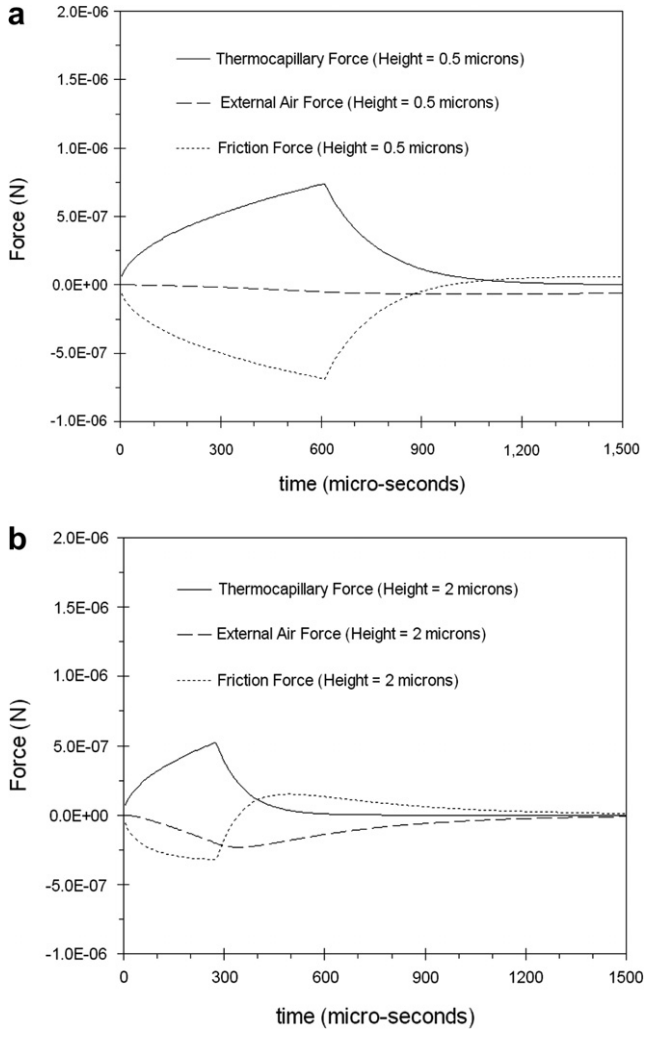

Fig. 8. Forces on droplet for varying channel heights.

forces have a similar trend as thermocapillary forces (see Fig. 7), except that the direction is opposite to the droplet motion. During both heating and cooling periods, the gas force is directed leftwards on the moving droplet, so its magnitude remains negative. The magnitude of the friction force changes signs, when the direction of droplet motion reverses. At the end of the cooling period, the direction of droplet movement reverses and the air volume begins expanding, so the magnitude of the external air force diminishes.

The net force on the micro-droplet (including thermocapillary, opposing gas pressure and frictional forces) is shown in Fig. 9. A large positive force is observed initially, due to the rapidly increasing thermocapillary force. Frictional resistance and opposing gas pressure forces are small before the droplet accelerates appreciably. The net force decreases with time, as the thermocapillary force is offset by rising frictional resistance when the droplet accelerates. After the heat source is removed, the thermocapillary force decreases quickly. As a result, the net force becomes negative and the droplet direction reverses. The external force

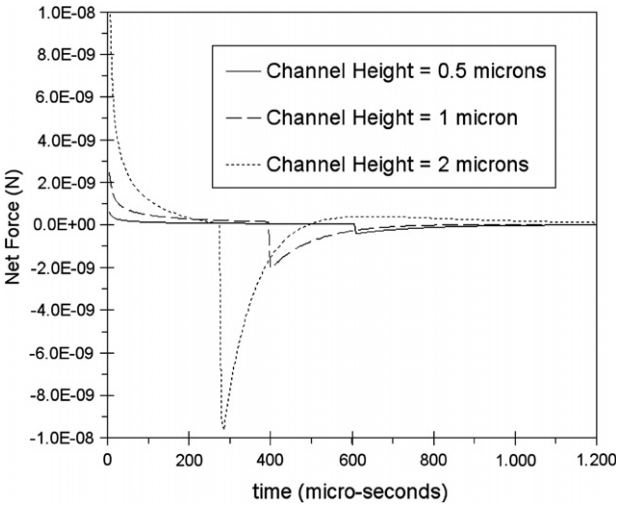

Fig. 9. Net force on droplet for varying channel heights.

decreases as the gas sections approach their initial conditions, so the magnitude of the net force decreases. These trends at varying microchannel sizes are illustrated in Fig. 9. The peak maximum negative force is delayed for smaller microchannels because higher internal frictional resistance reduces the droplet acceleration, thereby increasing the time required for the droplet to be displaced a specified amount and triggering the cooling period.

Close agreement between analytical and numerical predictions of droplet displacement in Fig. 10 provides further useful validation of the numerical model. The droplet motion has been generated by a stationary heat source in Fig. 1. Unlike past studies with a moving heat source at the receding edge of the droplet, the current study has shown that thermocapillary pumping can be sustained with a stationary heat source. But cycling of this heat source is needed for continuous operation of the micro-device. Otherwise, the micro-droplet would eventually become stationary at a new equilibrium position.

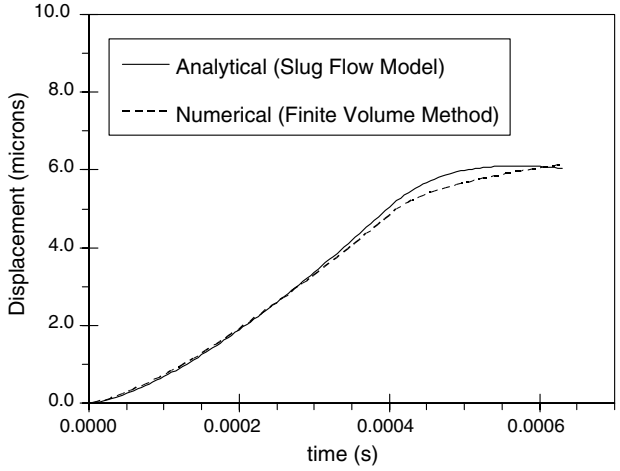

Fig. 10. Predicted droplet displacement.

5. Conclusions

This article concludes a two-paper set of companion papers, which focus on interfacial dynamics of an accelerating droplet in a closed microchannel. Both analytical and numerical formulations of heat transfer have been developed in this article. The temperature field within the droplet depends on heat exchange with the surrounding substrate and air regions. The 2-D transient energy equations are solved in the silicon substrate, thermal bridge and air regions. A thin air gap was placed between the thermal bridge and adjoining substrate, in order to reduce lateral heat losses through the thermal bridge. Numerical results have shown that a non-uniform interface pressure leads to spatial variations of temperature along the droplet/air interface. These results provide useful new insight for thermocapillary pumping of droplets in microchannels.

Acknowledgements

Support from the Natural Sciences and Engineering Research Council of Canada, as well as a University of Manitoba Graduate Fellowship (P. S. Glockner), is gratefully acknowledged.

References

[1] K. Vafai, L. Zhu, Analysis of a two-layered micro channel heat sink concept in electronic cooling, Int. J. Heat Mass Transfer 42 (1999) 2287–2297.

[2] S. Wu, J. Mai, Y.C. Tai, C.M. Ho, Micro heat exchanger using MEMS impinging jets, in: Proceedings of the 12th Annual International Workshop on Micro Electro Mechanical Systems, Orlando, FL, January 17–21, 1999, pp. 171–176.

[3] S. Whalen, M. Thompson, D. Bahr, C. Richards, R. Richards, Design, fabrication and testing of the P3 micro heat engine, Sensor. Actuator. 104 (2003) 200–208.

[4] N. Vandelli, D. Wroblewski, M. Velonis, T. Bifano, Development of a MEMS microvalve array for fluid flow control, J. Microelectromech. Syst. 7 (4) (1998) 395–403.

[5] A.D. Ketsdever, A.A. Green, E.P. Muntz, D.C. Wadsworth, S. Vargo, Heat transfer measurements and calculations for a MEMS fabricated resistojet: initial results, in: AIAA 34th Thermophysics Conference, Denver, CO, June 19–22, 2000.

[6] G.F. Naterer, Surface micro-profiling for reduced energy dissipation and exergy loss in convective heat transfer, Microscale Therm. Eng. 9 (3) (2005) 213–236.

[7] P. Dutta, A. Beskok, T.C. Warburton, Electro-osmotic flow control in complex microgeometries, J. Microelectromech. Syst. 11 (1) (2002) 36–44.

[8] E.Y.K. Ng, S.T. Poh, CFD analysis of double-layer microchannel conjugate parallel liquid flows with electric double layer effects, Numer. Heat Transfer A–Appl. 40 (7) (2001) 735–749.

[9] S. Ghosal, Lubrication theory for electro-osmotic flow in a microfluidic channel of slowly varying cross-section and wall charge, J. Fluid Mech. 459 (1) (2002) 103–128.

[10] P.S. Glockner, G.F. Naterer, Numerical simulation of electrokinetic flow and heat transfer in microchannels with a finite volume method, Numer. Heat Transfer A–Appl. 49 (5) (2006) 451–470.

[11] G.F. Naterer, O.B. Adeyinka, Microfluidic exergy loss in a non-polarized thermomagnetic field, Int. J. Heat Mass Transfer 48 (2005) 3945–3956.

[12] G.F. Naterer, J.A. Camberos, Entropy and the second law in fluid flow and heat transfer simulation, AIAA J. Thermophys. Heat Transfer 17 (2003) 360–371.

[13] G.F. Naterer, Heat Transfer in Single and Multiphase Systems, CRC Press, Boca Raton, FL, 2002.

[14] J. Lee, C.J. Kim, Liquid micromotor driven by continuous electrowetting, in: Proceedings of IEEE MEMS Conference, Heidelberg, Germany, 1998, pp. 538–543.

[15] K.S. Yun, J. Cho, J. Bu, C.J. Kim, E. Yoon, A surface tension driven micropump for low voltage and low power operations, J. Microelectromech. Syst. 11 (5) (2002) 454–461.

[16] T.S. Sammarco, M.A. Burns, Heat transfer analysis of microfabricated thermocapillary pumping and reaction devices, J. Micromech. Microeng. 10 (2000) 42–55.

[17] T.S. Sammarco, M.A. Burns, Thermocapillary pumping of discrete drops in microfabricated analysis devices, AIChE J. 45 (1999) 350–366.

[18] S.M. Ghiaasiaan, R.C. Chedester, Boiling incipience in microchannels, Int. J. Heat Mass Transfer 45 (23) (2002) 4599–4606.

[19] R.C. Chedester, S.M. Ghiaasiaan, A proposed mechanism for hydrodynamically-controlled onset of significant void in microtubes, Int. J. Heat Fluid Flow 23 (6) (2002) 769–775.

[20] G.F. Naterer, W. Hendradjit, K.J. Ahn, J.E.S. Venart, Near-wall microlayer evaporation analysis and experimental study of nucleate pool boiling on inclined surfaces, ASME J. Heat Transfer 120 (3) (1998) 641–653.

[21] B.S. Dandapat, B. Santra, J.I. Andersson, Thermocapillarity in a liquid film on an unsteady stretching surface, Int. J. Heat Mass Transfer 46 (2003) 3009–3015.

[22] V. Ha, C. Lai, Onset of Marangoni instability of a two-component evaporating droplet, Int. J. Heat Mass Transfer 45 (26) (2002) 5143–5158.